

Numerical investigations on high-speed turbo-compressor rotor systems with air ring bearings: Nonlinear vibration behavior and optimization

P. Zeise^{a,*}, B. Schweizer^a

^a*Institute of Applied Dynamics, Technical University of Darmstadt, Otto-Berndt-Str. 2, 64287 Darmstadt, Germany*

Received 10 May 2023; accepted 7 November 2023

Abstract

Regarding aerodynamic bearings, mainly two basic types can be distinguished: air bearings with a rigid housing and air foil bearings with an elastic supporting structure. Here, a modified bearing concept – called air ring bearing – is investigated, which may be considered as a further development of rigid air bearings or as a combination of the two basic bearing types. The idea of air ring bearings is to insert a ring-shaped bearing bushing between the shaft and the foil structure. Alternatively, a visco-elastic supporting structure (e.g., an elastomer) can be applied to connect the bushing ring with the housing. In the first case, external dissipation is mainly generated by dry friction. In the latter case, viscous damping is used to provide external dissipation. Due to the external friction/damping generated by the ring mounting structure, rotor systems with air ring bearings can be operated above the linear threshold speed of instability so that stable self-excited vibrations with moderate amplitudes can be achieved in the complete speed range. Here, a detailed transient co-simulation model for rotor systems with air ring bearings is presented. The rotor is represented by a multibody model. The air films of the two bearings are represented by two nonlinear time-dependent finite element systems. The multibody model and the two finite element subsystems are solved simultaneously by means of an explicit sequential co-simulation technique. Due to the strong nonlinearities, the system shows interesting vibration and bifurcation effects, which are investigated in detail with the help of run-up simulations.

© 2023 University of West Bohemia.

Keywords: air ring bearing, nonlinear rotor dynamics, co-simulation model, optimization

1. Introduction

Air bearings may be used in many technical applications, particularly in cases where oil-free operating conditions are necessary. They may be subdivided into two classes: (i) air bearings with a rigid housing and (ii) air foil bearings. Rigid air bearings have a rigid bearing housing and the air film is generated between the rotor journal and the inner bearing surface. The bearing properties (e.g., load capacity) and the dynamic behavior of the rotor/bearing system are mainly determined by the bore geometry [1]. Applying a plain cylindrical bore geometry usually entails a poor rotordynamic stability behavior, i.e., the rotor gets unstable at very low rotor speeds. Stability of the rotor/bearing system can be improved by using a multi-lobe bore geometry and especially by applying a herringbone geometry [13,23,39]. Foil bearings usually consist of a top foil and a compliant substructure [28]. As a consequence, the air gap between the rotor journal and the top foil is depending on the top foil deformation. With respect to the elastic substructure, foil bearings can be subdivided into different categories. Often bump foils [3,15,22] are used as

*Corresponding author. Tel.: +49 615 116 234 61, e-mail: zeise@ad.tu-darmstadt.de.
<https://doi.org/10.24132/acm.2023.836>

compliant substructure. Alternatively, beam foils [9], a metal mesh [29], springs [35] or wing foils [36] can be applied. The dynamic behavior of foil bearings is investigated experimentally and numerically in [4, 7, 16, 19, 27], for instance. Numerical and experimental studies on the lift-off speed can, for instance, be found in [2, 20]. Thermal models for air foil bearings are, e.g., discussed in [21, 25, 30].

Properly designing air foil bearings, a stable operation (or at least self-excited oscillations with moderate amplitudes) of the rotor system can be achieved within the considered speed range. Foil bearings are rather robust and frequently applied in practice. Calculation models for foil bearings are extraordinary involved. The numerical prediction of the stability of rotor systems with air foil bearings is very complicated. The dynamical behavior of such systems can even change during the operation due to wear in the top-foil coating. Regarding bearings with a rigid housing, the bore geometry has to be chosen carefully to achieve a stable rotor behavior. Due to the low viscosity of air, rigid air bearings frequently suffer from a reduced stability behavior. Even if a multi-lobe bore geometry is used, instability problems may occur already for low rotor speeds. Stable operation above the (linear) threshold speed of instability is usually not possible due to the very small damping property of air. To obtain a stable rotor behavior, frequently rigid bearings with a herringbone-geometry are used [6, 10, 17, 23, 39]. While herringbone bearings often provide an excellent rotor stability, they suffer from different technical problems (e.g., small clearances, involved thermo-management, manufacturing costs).

Air ring bearings can be an interesting alternative to air foil bearings and rigid air bearings. They can be considered as a simple and very obvious further development of rigid air bearings. The idea is simply to mount the bearing bushing with an elastomer [26, 38, 40], with a flexible membrane [5], springs [34] or with a foil structure [41] in the housing, see Fig. 1. The elastomer (foil structure) provides additional external damping (friction) to the rotor system so that the vibration behavior is improved. Properly designed air ring bearings may provide a stable rotor operation within the complete speed range or at least self-excited oscillations with moderate amplitudes. Here, air ring bearings with a three-lobe bore geometry are considered, where the ring is visco-elastically mounted in the housing (elastomer). Ring bearings mounted in a foil structure are, for instance, treated in [41].

The vibration and bifurcation behavior of rotor systems with air ring bearings is rather interesting. Typically, three different bifurcation paths may be detected for high-speed rotors supported in air ring bearings:

- For the case that the supporting structure of the ring is rather stiff and the external damping/friction low, *bifurcation path 1* is observed. This bifurcation path is dangerous and

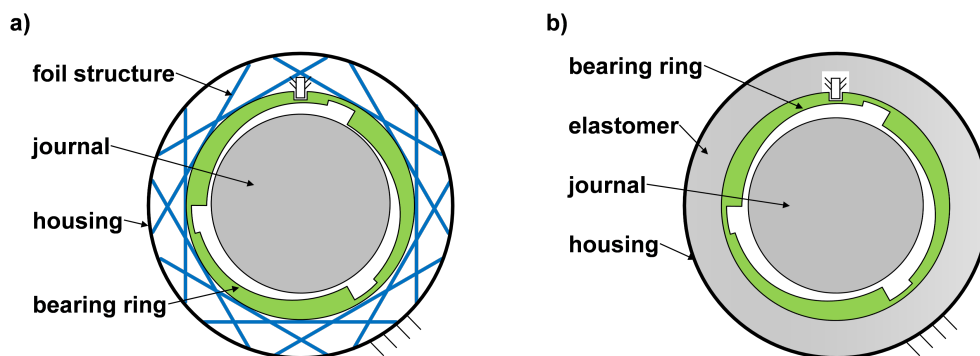


Fig. 1. Air ring bearing with (a) foil structure and (b) elastomer (visco-elastic mounting), see [41]

has to be omitted by a proper design of the rotor/bearing system, because self-excited oscillations with very large amplitudes are detected.

- For moderate ring stiffnesses and larger ring damping/friction, the harmless *bifurcation path 2a* is observed, where self-excited vibrations with moderate amplitudes occur.
- For very low ring stiffnesses, low damping and rather large ring masses, *bifurcation path 2b* can be detected, which should also be prevented in technical applications due to large rotor amplitudes.

It should be stressed that the basin of attraction for *bifurcation path 2a* is typically relatively large. Therefore, the rotor and especially the bearing parameters can in practice be determined in such a way that *bifurcation path 1* and *bifurcation path 2b* can be omitted.

The new contributions of this work are:

- The influence of the bore geometry of the inner ring surface on the stability and bifurcation behavior is analyzed in detail by numerical run-up simulations. Specifically, the effect of the nominal bearing clearance and the slope of the lobes is investigated.
- In [41], only the influence of the stiffness and damping of the ring supporting structure on the rotordynamic behavior has been analyzed. Here, comprehensive numerical studies are presented, where the effect of the bearing bore geometry on the system dynamics is examined.
- It is shown that both parameters – nominal bearing clearance and lobe geometry – have a very significant influence on the vibration and bifurcation behavior of the system.
- Based on the simulation results, practical design recommendations are given.

To carry out the run-up simulations, a detailed physical model for the air films is used, which are discretized by a finite element approach. The rotor is modeled as a 3D multibody system. The multibody model is coupled with the two finite element models of the air films with a co-simulation approach. With the coupled co-simulation model, the nonlinear system behavior is investigated.

The paper is organized as follows: The rotor/bearing co-simulation model is described in Section 2. The three bifurcation paths, typically observed in high-speed rotor systems with air ring bearings, are shortly recapped in Section 3. A detailed parameter and optimization study concerning the optimal choice of the air film geometry is presented in Section 4. The manuscript is concluded in Section 5.

2. Rotor/bearing simulation model of high-speed turbo compressor

2.1. Multibody model of the rotor

The considered rotor/bearing system is sketched in Fig. 2 and modelled as a multibody system, see [14, 32]. It is composed of the rotor shaft, the two wheels (compressor- and turbine-side wheel) and the two rigid bearing rings. In addition, two small imbalance masses are attached at the wheels. The axial coordinate z_{Rotor} characterizes the center of mass CM_{Rotor} of the complete rotor (shaft plus wheels). The middle planes of the turbine- and compressor-side bearing are defined by the axial coordinates z_{JT} and z_{JC} . The center of mass of the turbine CM_T and compressor wheel CM_C are termed by z_T and z_C , respectively.

For integrating the multibody system, the index-2 equations of motion (stabilized index-2 formulation according to [11]) are applied, which are given by

$$M(t, \boldsymbol{x})\dot{\boldsymbol{v}} = \boldsymbol{f}_e(t, \boldsymbol{x}, \boldsymbol{v}, \boldsymbol{u}_{\text{MBS}}) - \boldsymbol{G}^T(t, \boldsymbol{x})\boldsymbol{\lambda}, \quad (1)$$

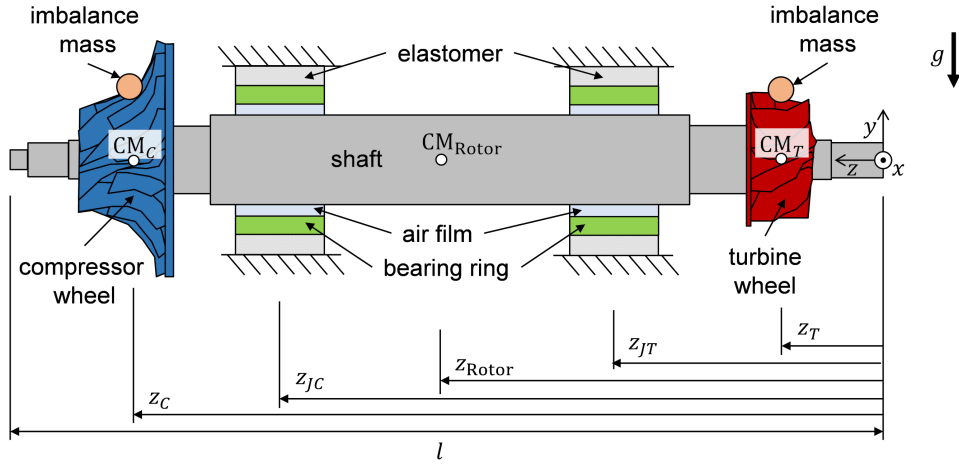


Fig. 2. High-speed rotor system: Turbo-compressor supported in two air ring bearings, see [41]

$$\mathbf{M}(t, \mathbf{x})\dot{\mathbf{x}} = \mathbf{M}(t, \mathbf{x})\mathbf{v} - \mathbf{G}^T(t, \mathbf{x})\boldsymbol{\mu}, \quad (2)$$

$$\mathbf{0} = \mathbf{g}(t, \mathbf{x}), \quad (3)$$

$$\mathbf{0} = \dot{\mathbf{g}}(t, \mathbf{x}, \mathbf{v}). \quad (4)$$

The vector $\mathbf{x} = [x_1, \dots, x_\kappa]^T \in \mathbb{R}^\kappa$ collects the κ (generalized) coordinates of the multibody system and the vector $\mathbf{v} = [v_1, \dots, v_\kappa]^T \in \mathbb{R}^\kappa$ the (generalized) velocities. $\mathbf{M}(t, \mathbf{x}) \in \mathbb{R}^{\kappa \times \kappa}$ is the mass matrix. The vector $\mathbf{f}_e(t, \mathbf{x}, \mathbf{v}, \mathbf{u}_{\text{MBS}})$ terms the externally applied forces/torques, the centrifugal and Coriolis forces. Gravity g acts in negative y -direction, see Fig. 2. Equation (1) are the force/torques balances. Equation (2) represents the kinematic differential equations, where the mass matrix is used as a scaling matrix to improve the numerical procedure [33]. The multibody system contains κ_c rheonomic algebraic constraint equations $g_i(t, \mathbf{x}) = 0$ ($i = 1, \dots, \kappa_c$), which are collected in the constraint vector $\mathbf{g} \in \mathbb{R}^{\kappa_c}$. The term $\mathbf{G}^T(t, \mathbf{x})\boldsymbol{\lambda}$ characterizes the constraint forces, where $\mathbf{G} = \partial\mathbf{g}/\partial\mathbf{x} \in \mathbb{R}^{\kappa_c \times \kappa}$ represents the constraint-Jacobian. The vector $\boldsymbol{\lambda} = [\lambda_1, \dots, \lambda_{\kappa_c}]^T \in \mathbb{R}^{\kappa_c}$ contains the Lagrange multipliers. According to the stabilized index-2 formulation [11], the algebraic constraint equations $\mathbf{0} = \dot{\mathbf{g}}(t, \mathbf{x}, \mathbf{v})$ on velocity level are included into the equations of motion with the help of the additional Lagrange multipliers $\boldsymbol{\mu} = [\mu_1, \dots, \mu_{\kappa_c}]^T \in \mathbb{R}^{\kappa_c}$. The input variables of the multibody system are collected in the vector $\mathbf{u}_{\text{MBS}}(t)$ and represent the resulting bearing forces of the two air films. It should be noted that the output vector $\mathbf{y}_{\text{MBS}}(t) = [\Delta\mathbf{r}_1^T, \Delta\dot{\mathbf{r}}_1^T, \Delta\mathbf{r}_2^T, \Delta\dot{\mathbf{r}}_2^T, \Omega]^T$ of the multibody subsystem consists of the angular velocity of the rotor and of the relative displacement and velocity coordinates of the compressor- and turbine-side journal. These output variables are directly used as input variables for the two finite element subsystems for calculating the resulting bearing forces of the two air films.

In this work, the ring is assumed to be connected to the housing by a visco-elastic material (elastomer). To simplify the analysis, an isotropic linear visco-elastic material is considered, which is described by the force law $\mathbf{F} = -c\mathbf{r}_R - d\dot{\mathbf{r}}_R$ with the stiffness coefficient c and the damping coefficient d .

2.2. Finite element model of the air film

Fig. 3 depicts the gap of the air film of an air ring bearing with a three-lobe geometry. The space-fixed x, y -reference system is placed in the center O of the bearing housing. It is assumed

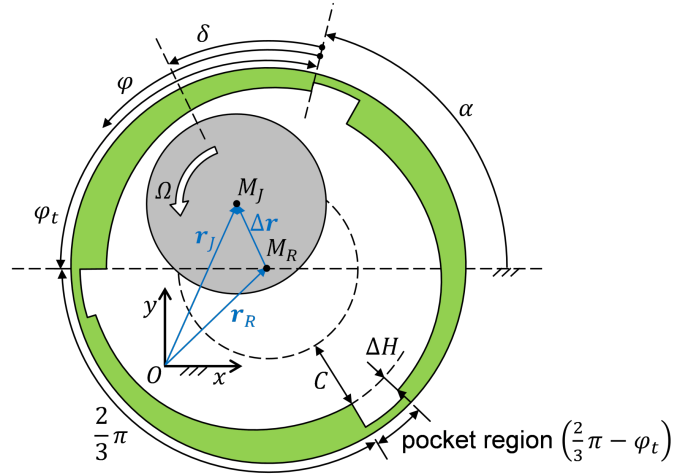


Fig. 3. Three-lobe air ring bearing geometry, see [41]

that the ring is able to move in x - and y -direction. The rotation around the z -axis is blocked (i.e., planar motion with two degrees of freedom). $\mathbf{r}_R = [x_R, y_R]^T$ is the position vector of the ring center M_R and $\mathbf{r}_J = [x_J, y_J]^T$ the position vector of the rotor journal M_J . The relative displacement vector of M_J with respect to M_R is denoted by $\Delta\mathbf{r} = \mathbf{r}_J - \mathbf{r}_R = [\Delta x, \Delta y]^T$. The relative velocity of M_J with respect to M_R is defined by $\Delta\dot{\mathbf{r}} = d/dt (\Delta\mathbf{r})$. Furthermore, ring-fixed polar coordinates $\Delta r = |\Delta\mathbf{r}|$ and $\delta = \text{atan2}(\Delta y, \Delta x) - \alpha$ are introduced, which time derivatives are given by $\dot{\Delta r} = 1/\Delta r (\Delta\mathbf{r} \cdot \Delta\dot{\mathbf{r}})$ and $\dot{\delta} = 1/\Delta r^2 (\Delta x \Delta \dot{y} - \Delta y \Delta \dot{x})$. The orientation of the ring relative to the housing is specified by the angle α ($\alpha = \text{const}$). The lobe region is defined by the angle φ_t . Three pockets are used for the air supply (circumferential extension $2\pi/3 - \varphi_t$). Here, ambient pressure is assumed. Moreover, C is the nominal clearance and ΔH the height of the step between the lobe region and the pocket. The angular coordinate φ , which is an auxiliary coordinate, is used for computing the pressure field with the Reynolds equation.

The pressure field $p(\varphi, z, t)$ in the air film is computed with the isothermal Reynolds equation for compressible fluids [18, 37]

$$\frac{1}{r^2} \frac{\partial}{\partial \varphi} \left(p h^3 \frac{\partial p}{\partial \varphi} \right) + \frac{\partial}{\partial z} \left(p h^3 \frac{\partial p}{\partial z} \right) = 6\Omega \eta \frac{\partial(p h)}{\partial \varphi} + 12\eta \frac{\partial(p h)}{\partial t}, \quad (5)$$

where the fluid is assumed to be an ideal gas described by the relationship $\varrho = p/(R_{\text{air}} T_{\text{air}})$ (R_{air} – specific gas constant of air, T_{air} – prescribed constant air film temperature), η terms the dynamic viscosity of air, $\varrho(\varphi, z, t)$ is the density field, Ω represents the rotor speed, r is the journal radius, $h(\varphi, t)$ describes the gap function and b denotes the bearing width. φ terms the circumferential and z the axial coordinate. The pressure is only computed in the lobe regions $S_{\text{lobe}} = \{[0, \varphi_t], [2\pi/3, 2\pi/3 + \varphi_t], [4\pi/3, 4\pi/3 + \varphi_t]\}$. Ambient pressure p_a is assumed in the pockets. The gap function h in the lobe regions is characterized by $h(\varphi) = C - \Delta r \cos(\varphi - \delta) + \Delta H \{1 + 2\pi/(3\varphi_t) [3\varphi/(2\pi)] - \varphi/\varphi_t\}$ with $\varphi \in S_{\text{lobe}}$, where $[\dots]$ denotes the floor function. Because journal misalignment is not considered here, symmetry boundary conditions can be applied with respect to the middle plane of the bearing for solving the Reynolds equation. At the remaining boundaries, the Dirichlet boundary condition $p = p_a$ is used.

The Reynolds equation is discretized with the help of a finite element approach, i.e., the time dependent pressure field $p(\varphi, z, t)$ is approximated by $\tilde{p}_i(\varphi, z, t) = \sum_{i=1}^{n_k} N_i(\varphi, z) p_i(t)$. $N_i(\varphi, z)$ represent the ansatz functions and $p_i(t)$ the pressure variables at the finite element nodes (n_k is the number of finite element nodes). Due to symmetry, only half the bearing needs to be discretized. Here, 360 finite elements (quadratic ansatz functions) are used, which result in $n_k = 1599$ pressure degrees of freedom. From the mathematical point of view, the discretized Reynolds equation represents a nonlinear ODE system (system of ordinary differential equations) for calculating the unknown pressure variables $p_i(t)$, which are arranged in the vector $\mathbf{p} = [p_1, \dots, p_{n_k}]^T$.

The nonlinear ODE system $\mathbf{f}(\mathbf{p}, \dot{\mathbf{p}}, t) = \mathbf{0}$ for the pressure variables $p_i(t)$ is solved with an implicit time integration algorithm. The global components $F_{px}(t)$, $F_{py}(t)$ of the resulting bearing forces are computed by an integration of the pressure field over the bearing surface

$$F_{px} = \int_0^{2\pi} \int_0^b p(\varphi, z) r \cos(\varphi + \alpha) dz d\varphi, \quad (6)$$

$$F_{py} = \int_0^{2\pi} \int_0^b p(\varphi, z) r \sin(\varphi + \alpha) dz d\varphi. \quad (7)$$

The output variables of the finite element subsystem are the resultant bearing forces. They are arranged in the output vector $[F_{px}, F_{py}]^T$. The rotor speed Ω and the relative journal displacement vector $\Delta\mathbf{r} = [\Delta x, \Delta y]^T$ in combination with its time derivative $\Delta\dot{\mathbf{r}} = [\Delta\dot{x}, \Delta\dot{y}]^T$ define the input variables of the finite element subsystem. Because the rotor system has two air films, the two output vectors $\mathbf{y}_{\text{FEM1}} = [F_{px1}, F_{py1}]^T$ and $\mathbf{y}_{\text{FEM2}} = [F_{px2}, F_{py2}]^T$ and the resulting output vector $\mathbf{y}_{\text{FEM}} = [F_{px1}, F_{py1}, F_{px2}, F_{py2}]^T$ are introduced. The output variables \mathbf{y}_{FEM} of the finite element subsystems are the input variables \mathbf{u}_{MBS} for the multibody subsystem ($\mathbf{u}_{\text{MBS}} = \mathbf{y}_{\text{FEM}}$).

Final remark on the calculation of the bearing forces: The bearing forces according to (6) and (7) represent pure hydrodynamic forces. If the bearing eccentricities become large, the gap height $h(\varphi, t)$ between rotor and journal may get very small so that mixed lubrication effects occur. Then, a mere hydrodynamic approach based on the Reynolds equation will not be sufficient.

Here, a straightforward mixed lubrication approach has been applied [2, 3, 8, 37]. If the distance between the ring and the journal gets below a critical value – i.e., if the gap function $h(\varphi, t)$ is locally smaller than the user-defined value h_{con} – mixed lubrication is assumed to occur at this gap point. In this work, h_{con} has been set to $0.04C$. At gap points where $h(\varphi, t) \leq h_{\text{con}}$, additional contact forces at journal and ring are superimposed to the pure hydrodynamic forces resulting from the Reynolds equation. The mechanical approach used here for the asperity contact forces of the two contacting surfaces is described by a penalty force model with a penalty stiffness of $c_{\text{con}} = 10^7 \text{ N mm}^{-3}$.

The simulations in Sections 3 and 4 have shown that mixed lubrication only very rarely occurs with the actual rotor/bearing system. Even in whirl/whip regions with large bearing eccentricities, no mechanical contact is observed between ring and rotor journal as can, for instance, be seen in the orbit plots in Section 3.

2.3. Linearization and modal analysis

The considered rotor/bearing system is highly nonlinear. Nevertheless, different characteristic vibration mode shapes and corresponding frequencies – excited by the rotor imbalance and especially by the whirl/whip frequencies of the air films – can be observed in the frequency spectra of run-up simulations. To get a closer insight into these vibration modes, the rotor/bearing system is linearized and an eigenmode analysis is carried out. For that purpose, the air films have to be linearized. The stiffness behavior of the air film is highly nonlinear and a function of the bearing eccentricity. Fig. 4 depicts an approximate calculation of the radial film stiffness as a function of the relative journal displacement $\varepsilon = |[0, -\Delta y]^T|/C$ for $C = 20 \mu\text{m}$, $\Delta H = 40 \mu\text{m}$, $\Omega = 1000 \text{ Hz}$ and different values of Δy .

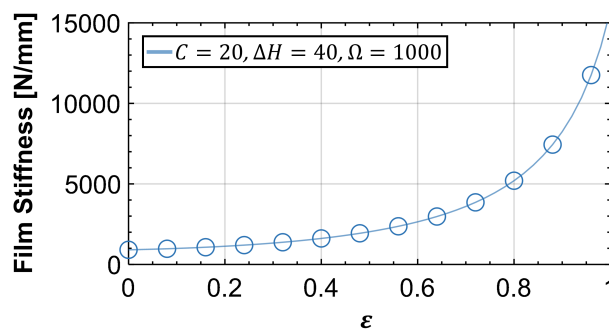


Fig. 4. Approximate calculation of the radial air film stiffness as a function of the bearing eccentricity ε

It should be noted that the rotor is rather stiff (shaft radius $r = 15 \text{ mm}$) and may therefore be regarded as a rigid body. The first free-free bending eigenfrequency of the rotor is $\approx 2600 \text{ Hz}$ and well above the maximum rotor speed of 2000 Hz . Furthermore, it should be mentioned that damping effects have been neglected in the eigenmode analysis. Finally, it should be stressed that tilting of the rings is not considered in the calculation, since the rings can only move in the x, y -plane in our model.

For the eigenmode analysis, the ring mounting stiffness and the ring damping parameter have been set to $c = 500 \text{ N mm}^{-1}$ and $d = 0 \text{ N s m}^{-1}$, respectively. The air film of each bearing has been replaced by two linear springs acting in x - and y -direction with spring constants $c_{\text{air},x} = c_{\text{air},y} = 2000 \text{ N mm}^{-1}$ (estimated air film stiffness for $\varepsilon \approx 0.5$). The results of the eigenmode calculation are (see Fig. 5):

- *Mode_1(b)* and *Mode_1(f)* are conical modes with a vibration node at the compressor-side bearing (backward mode *Mode_1(b)* $\approx 125 \text{ Hz}$; forward mode *Mode_1(f)* $\approx 145 \text{ Hz}$).
- *Mode_2(b)* and *Mode_2(f)* are conical modes with a vibration node at the turbine-side bearing (backward mode *Mode_2(b)* $\approx 156 \text{ Hz}$; forward mode *Mode_2(f)* $\approx 181 \text{ Hz}$).
- *Mode_3(b)* and *Mode_3(f)* are conical modes with a vibration node at the compressor-side bearing (backward mode *Mode_3(b)* $\approx 1161 \text{ Hz}$; forward mode *Mode_3(f)* $\approx 1162 \text{ Hz}$).
- *Mode_4(b)* and *Mode_4(f)* are conical modes with a vibration node at the turbine-side bearing (backward mode *Mode_4(b)* $\approx 1176 \text{ Hz}$; forward mode *Mode_4(f)* $\approx 1179 \text{ Hz}$).

2.4. Co-simulation model of the overall system

The coupled system consisting of the rotor and the two bearings is integrated in the time domain using a co-simulation approach [12, 24, 31]. Therefore, the overall system is decomposed

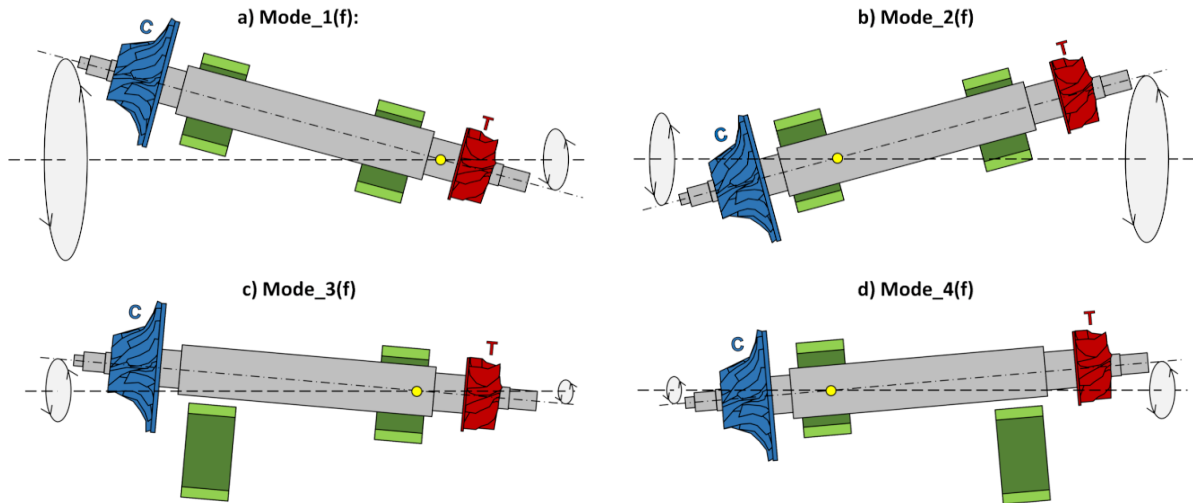


Fig. 5. Rigid body forward mode shapes

into three different subsystems. The first subsystem (multibody subsystem, MBS) contains the rotor. The second and third subsystems are the two finite element subsystems of the discretized Reynolds equations (FEM1 and FEM2).

To accomplish the co-simulation, appropriate coupling variables have to be introduced (input/output variables, see above). They characterize the mathematical connection between the three subsystems. Moreover, a communication-time grid has to be defined. Therefore, the macro-time points T_N ($N = 0, 1, 2, \dots$) are introduced. In the framework of a co-simulation, the subsystems can be integrated independently within the macro-step $T_N \rightarrow T_{N+1}$. Information, i.e., coupling variables, are interchanged only at the macro-time points. Within the macro-interval $[T_N, T_{N+1}]$, the coupling variables are approximated. Therefore, appropriate extrapolation and interpolation polynomials are used.

Here, an explicit co-simulation technique, namely the sequential Gauss-Seidel scheme, is used. In the current implementation, the multibody subsystem is considered as the master subsystem.

3. Simulation results: Basic bifurcation behavior

All simulations in Section 3 have been accomplished with the following parameters: $m = 830$ g, inertia tensor $\mathbf{J}_{\text{Rotor}} = \text{diag}(2\,500 \text{ kg mm}^2, 2\,500 \text{ kg mm}^2, 120 \text{ kg mm}^2)$ with respect to the center of mass, journal radius $r = 15$ mm, $l = 250$ mm, $z_{\text{Rotor}} = 125$ mm, $z_{JC} = 170$ mm, $z_{JT} = 60$ mm, $m_R = 50$ g ($m_R = 150$ g in Section 3.3), ring width $b = 28.6$ mm. The bearing parameters are: air viscosity $\eta_{\text{air}} = 20.936 \times 10^{-6} \text{ kg m}^{-1} \text{ s}^{-1}$ (assumed fluid temperature: $T_{\text{air}} = 80^\circ \text{ C}$), bearing clearance $C = 20 \mu\text{m}$ (warm clearance; rotor expansion due to centrifugal forces is neglected), step height $\Delta H = 40 \mu\text{m}$, lobe angle $\varphi_t = 110^\circ$, ring orientation angle $\alpha = \pi - \varphi_t$. To analyze the possible bifurcations of the high-speed rotor/bearing system, the stiffness parameter c as well as the damping parameter d are varied. At the beginning of the run-up simulations, the rotor and the two rings are centered at the space-fixed z -axis and zero velocity is assumed. The rotor speed $\Omega(t)$ is linearly increased. The maximum speed of 2 000 Hz is reached in 3 s, i.e., $\Omega(t) = 2\pi/3 \cdot 2\,000t \text{ s}^{-2}$. To discuss the occurring bifurcations of the system vividly, the rotor unbalance is assumed to be zero. The effect of imbalance on the dynamical behavior of the system is discussed in [41].

3.1. Rotor run-up simulation: Bifurcation path 1

Simulation results of a rotor run-up with the parameters $c = 1\,000\text{ N mm}^{-1}$ and $d = 50\text{ N s m}^{-1}$ are arranged in Fig. 6. The figure depicts the dimensionless bearing eccentricities $\varepsilon_C = \Delta r_C/C$ and $\varepsilon_T = \Delta r_T/C$ of the compressor- and turbine-side bearing, the vertical displacement of the compressor $y_{JC}(t)$ and turbine wheel $y_{JT}(t)$ and the corresponding frequency spectra. Note that the dimensionless eccentricities ε_C and ε_T are defined by using the minimal clearance C . Since the maximum clearance is $C + \Delta H$ at the beginning of the lobe regions, ε_C and ε_T can get larger than 1 without the journal contacting the ring. The figure also contains compressor- and turbine-side orbit plots of the relative journal displacements $\Delta r_C(t)$ and $\Delta r_T(t)$. It should be mentioned that the three green spirals represent the three lobes of the inner ring surface.

- In the range $0 \leq t \leq 1\,150\text{ ms}$ ($0 \leq \Omega \leq 767\text{ Hz}$), the rotor is rotating in a stable equilibrium position.

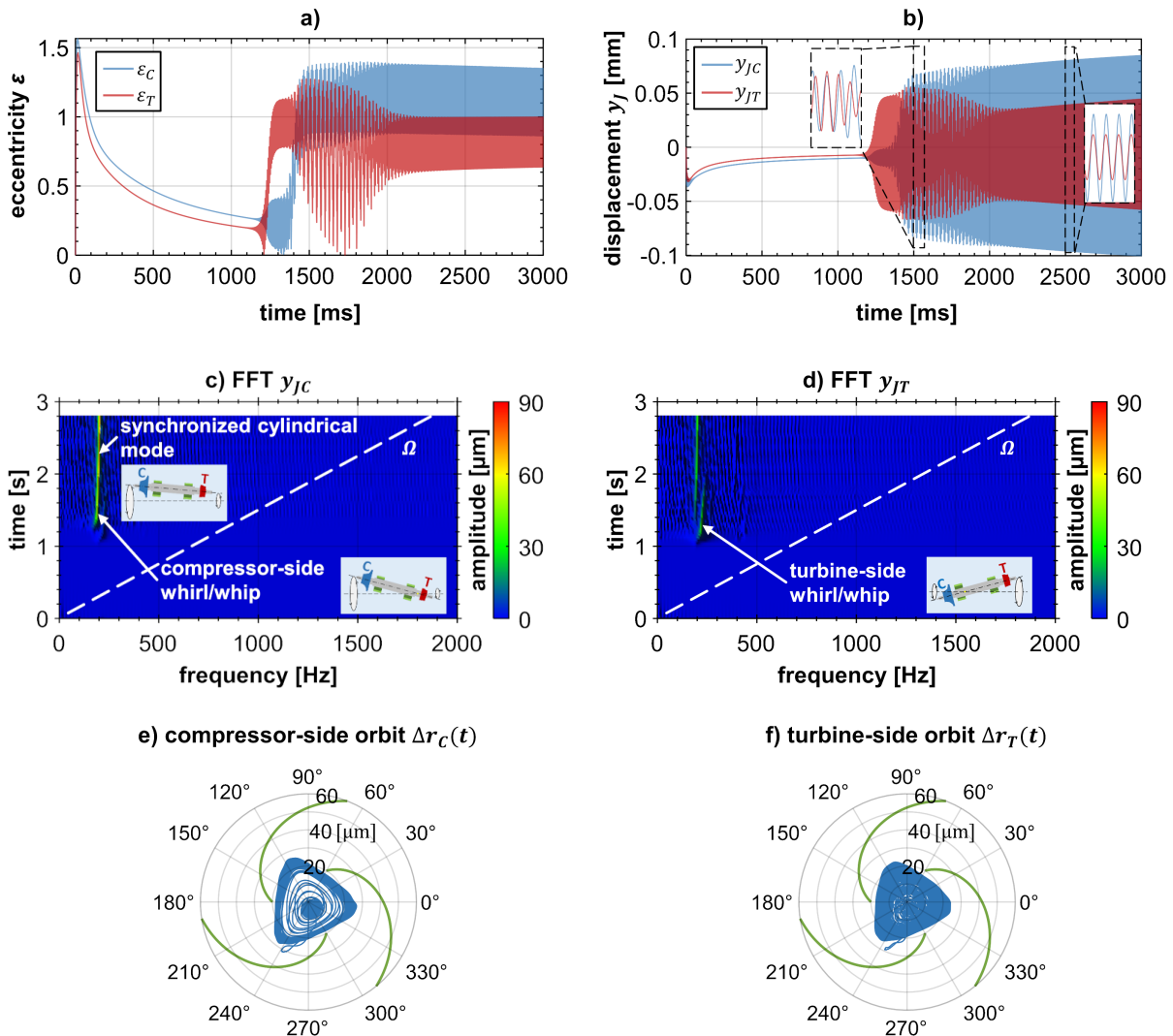


Fig. 6. Bifurcation path 1 with $c = 1\,000\text{ N mm}^{-1}$, $d = 50\text{ N s m}^{-1}$: (a) dimensionless bearing eccentricities $\varepsilon_C(t)$ and $\varepsilon_T(t)$, (b) vertical journal displacements $y_{JC}(t)$ and $y_{JT}(t)$, (c) frequency spectrum of $y_{JC}(t)$, (d) frequency spectrum of $y_{JT}(t)$, (e)–(f) compressor- and turbine-side orbit plots of the relative journal displacements $\Delta r_C(t)$ and $\Delta r_T(t)$

- At $t \approx 1\,150$ ms, the equilibrium position becomes unstable by means of a Hopf bifurcation and stable quasiperiodic oscillations are observed (so-called whirl/whip vibrations). Firstly, a whirl/whip primarily generated by the turbine-side bearing is observed. At $t \approx 1\,350$ ms, also a whirl/whip produced by the compressor-side bearing is detected.
- At $t \approx 2\,100$ ms, a synchronization effect takes place: the turbine-side whirl/whip frequency shows a jump and synchronizes with the compressor-side whirl/whip. Then, the synchronized whirls/whips are exciting a cylindrical forward mode.
- Further increasing the speed of the rotor system has only little influence on the frequencies and the amplitudes.
- Since the bearing eccentricities and the rotor amplitudes are typically very large in connection with bifurcation path 1, a secure operation of the rotor/bearing system is usually not possible within bifurcation path 1.

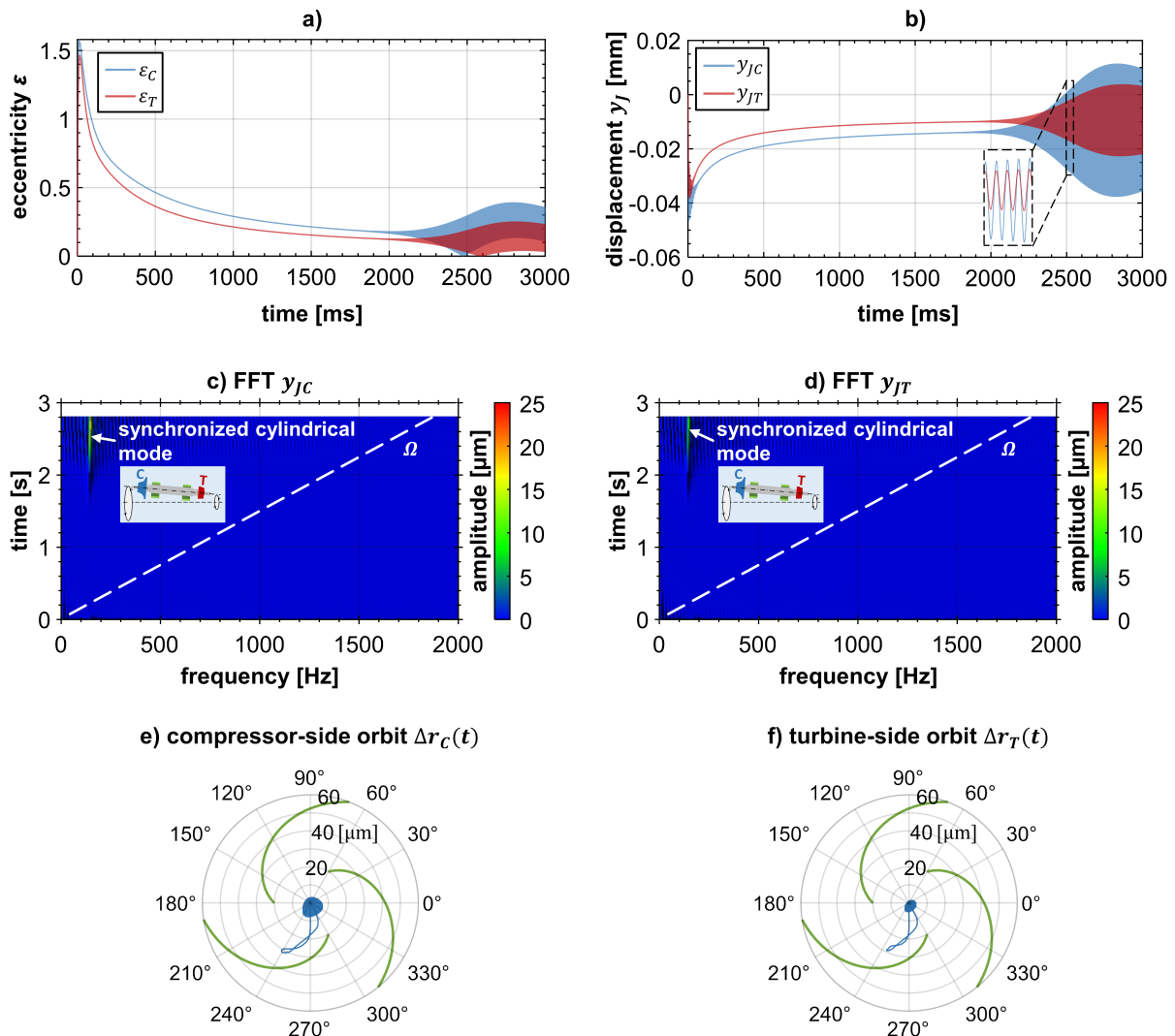


Fig. 7. Bifurcation path 2a with $c = 500 \text{ N mm}^{-1}$, $d = 50 \text{ N s m}^{-1}$: (a) dimensionless bearing eccentricities $\varepsilon_C(t)$ and $\varepsilon_T(t)$, (b) vertical journal displacements $y_{JC}(t)$ and $y_{JT}(t)$, (c) frequency spectrum of $y_{JC}(t)$, (d) frequency spectrum of $y_{JT}(t)$, (e)–(f) compressor- and turbine-side orbit plots of the relative journal displacements $\Delta r_C(t)$ and $\Delta r_T(t)$

3.2. Rotor run-up simulation: Bifurcation path 2a

For this run-up simulation, the stiffness is decreased to $c = 500 \text{ N mm}^{-1}$. The damping coefficient remains $d = 50 \text{ N s m}^{-1}$. The results are collected in Fig. 7.

- At $t \approx 2000 \text{ ms}$, the rotor equilibrium position becomes unstable. A stable whirl/whip vibration is detected. The amplitudes of the whirl/whip are rather low so that the system can be run safely in the whirl/whip regime, i.e., in the complete speed range.
- Here, the compressor- and the turbine-side whirl/whip have the same frequency.

3.3. Rotor run-up simulation: Bifurcation path 2b

Now, the stiffness is further decreased to $c = 100 \text{ N mm}^{-1}$. The damping coefficient is again $d = 50 \text{ N s m}^{-1}$. It should be mentioned that the mass of the ring has been increased to $m_R = 150 \text{ g}$ in this run-up simulation. The simulation results can be seen in Fig. 8.

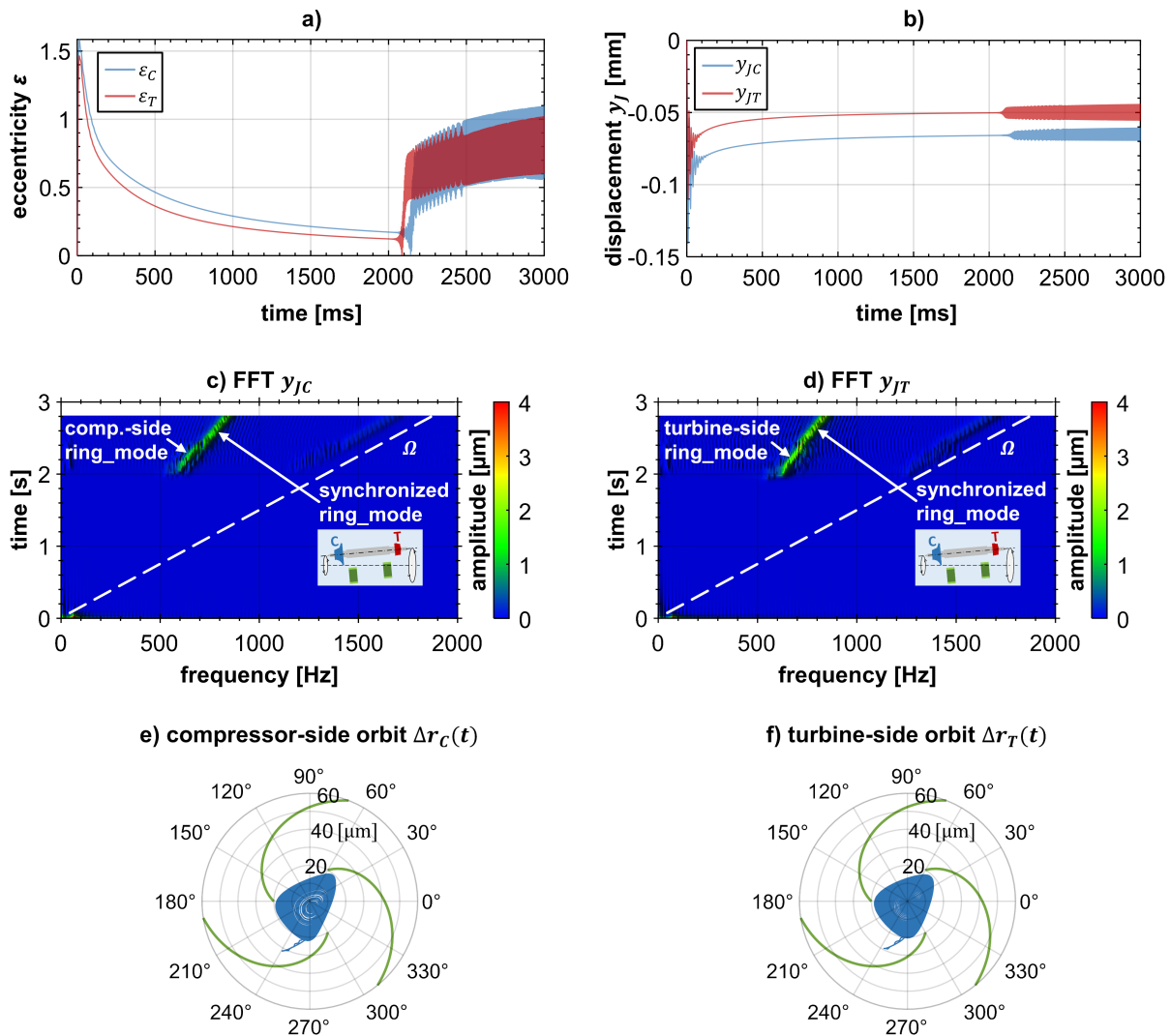


Fig. 8. Bifurcation path 2b with $c = 100 \text{ N mm}^{-1}$, $d = 50 \text{ N s m}^{-1}$, $m_R = 150 \text{ g}$: (a) dimensionless bearing eccentricities $\varepsilon_C(t)$ and $\varepsilon_T(t)$, (b) vertical journal displacements $y_{JC}(t)$ and $y_{JT}(t)$, (c) frequency spectrum of $y_{JC}(t)$, (d) frequency spectrum of $y_{JT}(t)$, (e)–(f) compressor- and turbine-side orbit plots of the relative journal displacements $\Delta r_C(t)$ and $\Delta r_T(t)$

- At $t \approx 2050$ ms, the equilibrium position becomes unstable by means of a Hopf bifurcation and self-excited vibrations are observed. Here, the whirl/whip frequencies of the two air films excite special ring mode shapes [41]. In the range $2050 \text{ ms} \leq t \leq 2500 \text{ ms}$, the frequencies of the whirls/whips generated by the two bearings are almost equal.
- As the rotor speed increases, the bearing eccentricities rise to a critical level. The whirl/whip frequencies increase almost linearly with the rotor speed. Since the bearing eccentricities are usually very large in connection with bifurcation path 2b, a secure operation of the rotor/bearing system within bifurcation path 2b is generally not possible.
- For $t > 2500$ ms, the frequencies of the whirls/whips are identical (i.e., a full synchronization occurs). A cylindrically-shaped ring mode shape is observed.

4. Parameter studies and optimization

As mentioned above, a three-lobe bearing geometry is used here, which is mainly specified by the bearing clearance C (warm clearance) and the step height ΔH . In this section, C and

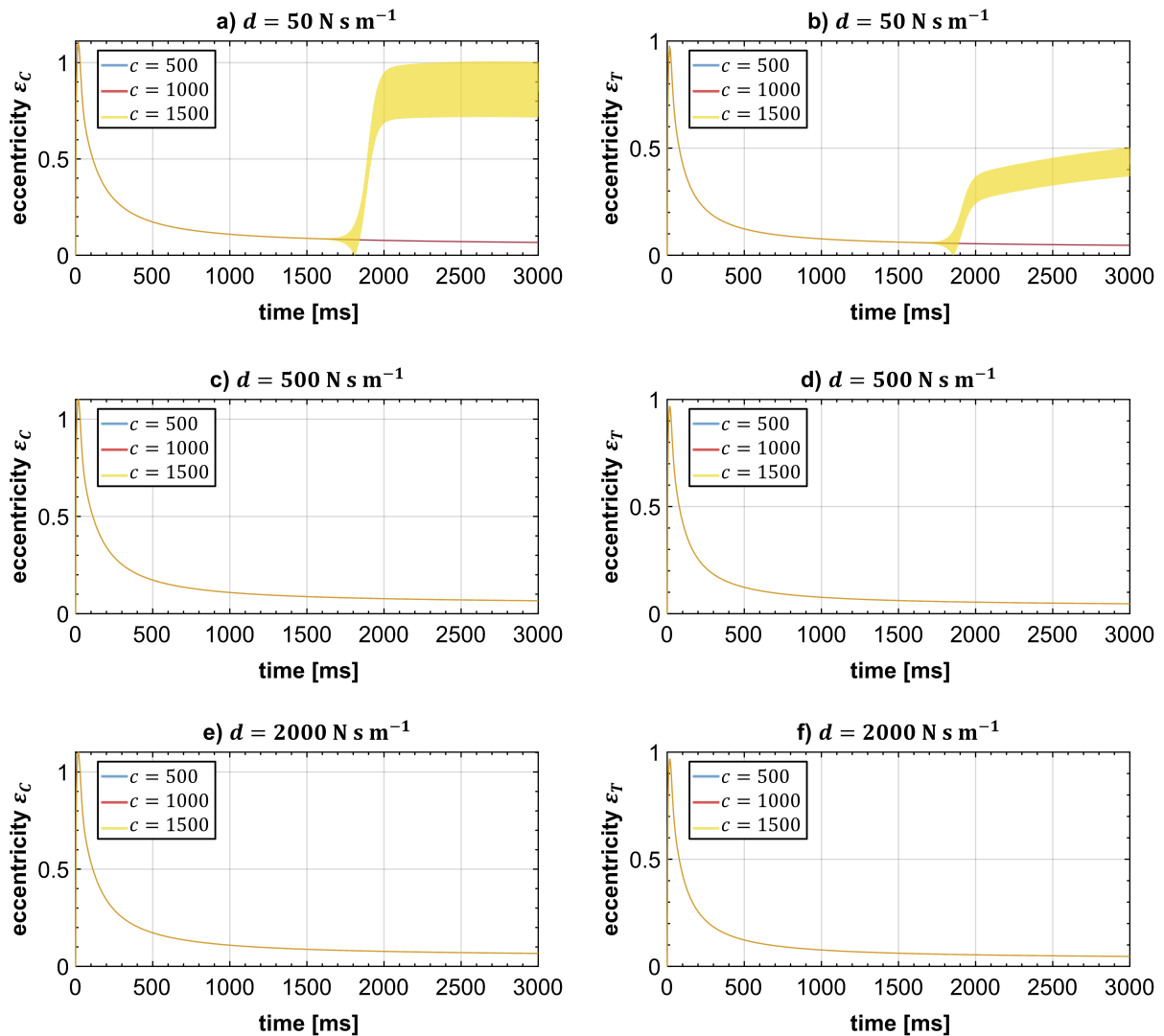


Fig. 9. Case 1 ($C = 10 \mu\text{m}$, $\Delta H = 20 \mu\text{m}$), compressor- and turbine-side bearing eccentricities $\varepsilon_C(t)$ and $\varepsilon_T(t)$: (a)–(b) $d = 50 \text{ N s m}^{-1}$, (c)–(d) $d = 500 \text{ N s m}^{-1}$, (e)–(f) $d = 2000 \text{ N s m}^{-1}$

ΔH are varied in order to study their influence on the bifurcation behavior of the rotor/bearing system.

Case 1: Fig. 9 shows the compressor- and turbine-side bearing eccentricities for $C = 10 \mu\text{m}$ and $\Delta H = 20 \mu\text{m}$ for three different elastomer stiffnesses c (1500 N mm^{-1} , 1000 N mm^{-1} , 500 N mm^{-1}) and three different damping parameters d (2000 N s m^{-1} , 500 N s m^{-1} , 50 N s m^{-1}). As can be seen, all simulations are stable (rotor rotation around a stable equilibrium point) with only one exception: for the case $c = 1500 \text{ N mm}^{-1}$ in combination with the very low damping $d = 50 \text{ N s m}^{-1}$, the critical *bifurcation path I* is detected. The corresponding vertical displacements of the compressor $y_{JC}(t)$ and turbine wheel $y_{JT}(t)$ are collected in Fig. 10 and also corresponding frequency spectra for the parameters $d = 50 \text{ N s m}^{-1}$ and $c = 1500 \text{ N mm}^{-1}$. Since the run-up simulations have been carried out with zero imbalance, the stable simulations do not exhibit any vibrations so that the frequency spectra become trivial. If imbalance would be taken into account, stable imbalance vibrations around the equilibrium position would be observed (at least for small imbalances). The frequency spectra for $d = 50 \text{ N s m}^{-1}$ and $c = 1500 \text{ N mm}^{-1}$ only exhibit a subsynchronous frequency resulting from the whirl/whip motion. Of course, if

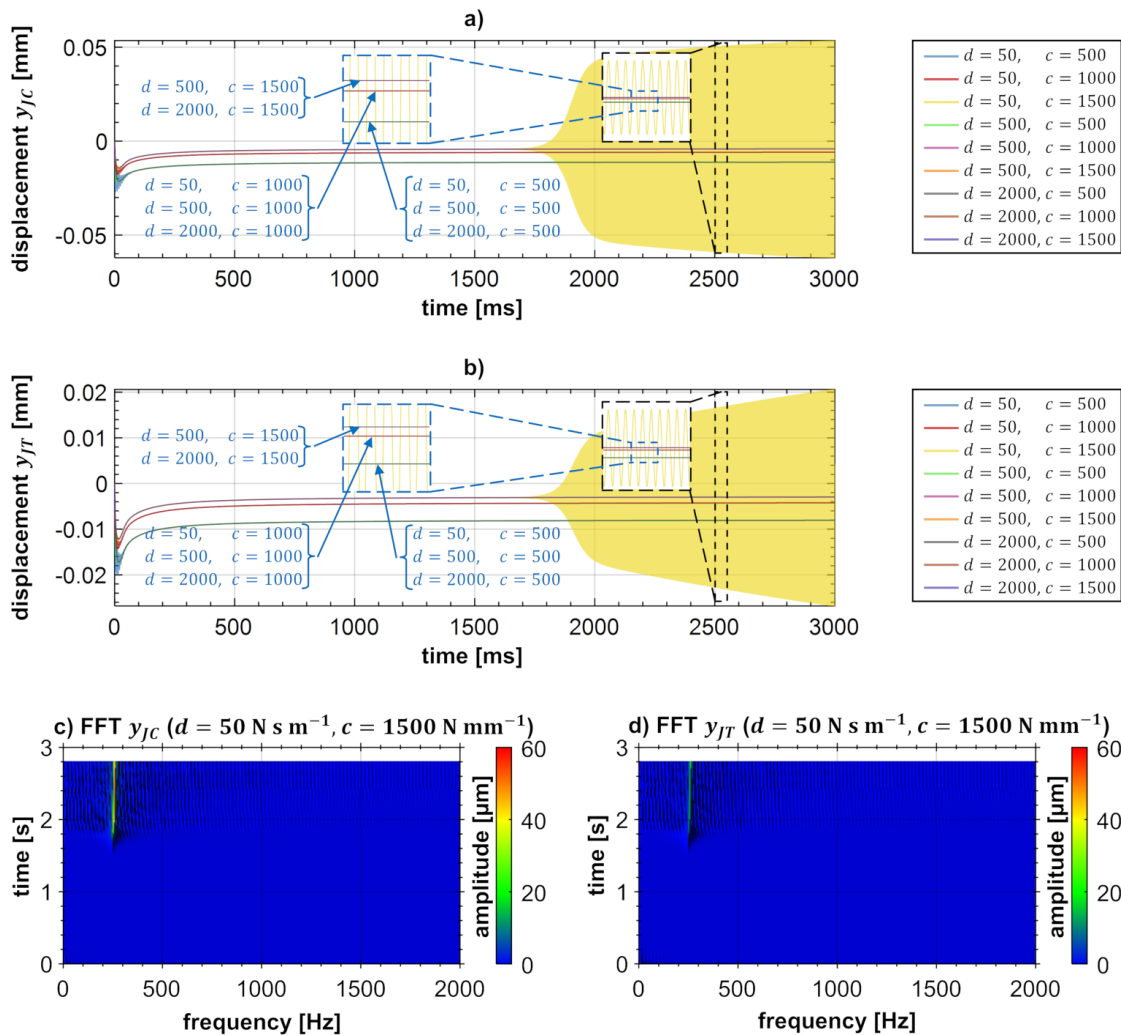


Fig. 10. Case 1 ($C = 10 \mu\text{m}$, $\Delta H = 20 \mu\text{m}$): (a)–(b) compressor and turbine-side rotor displacements $y_{JC}(t)$ and $y_{JT}(t)$, (c)–(d) frequency spectra of $y_{JC}(t)$ and $y_{JT}(t)$ for the parameters $d = 50 \text{ N s m}^{-1}$ and $c = 1500 \text{ N mm}^{-1}$

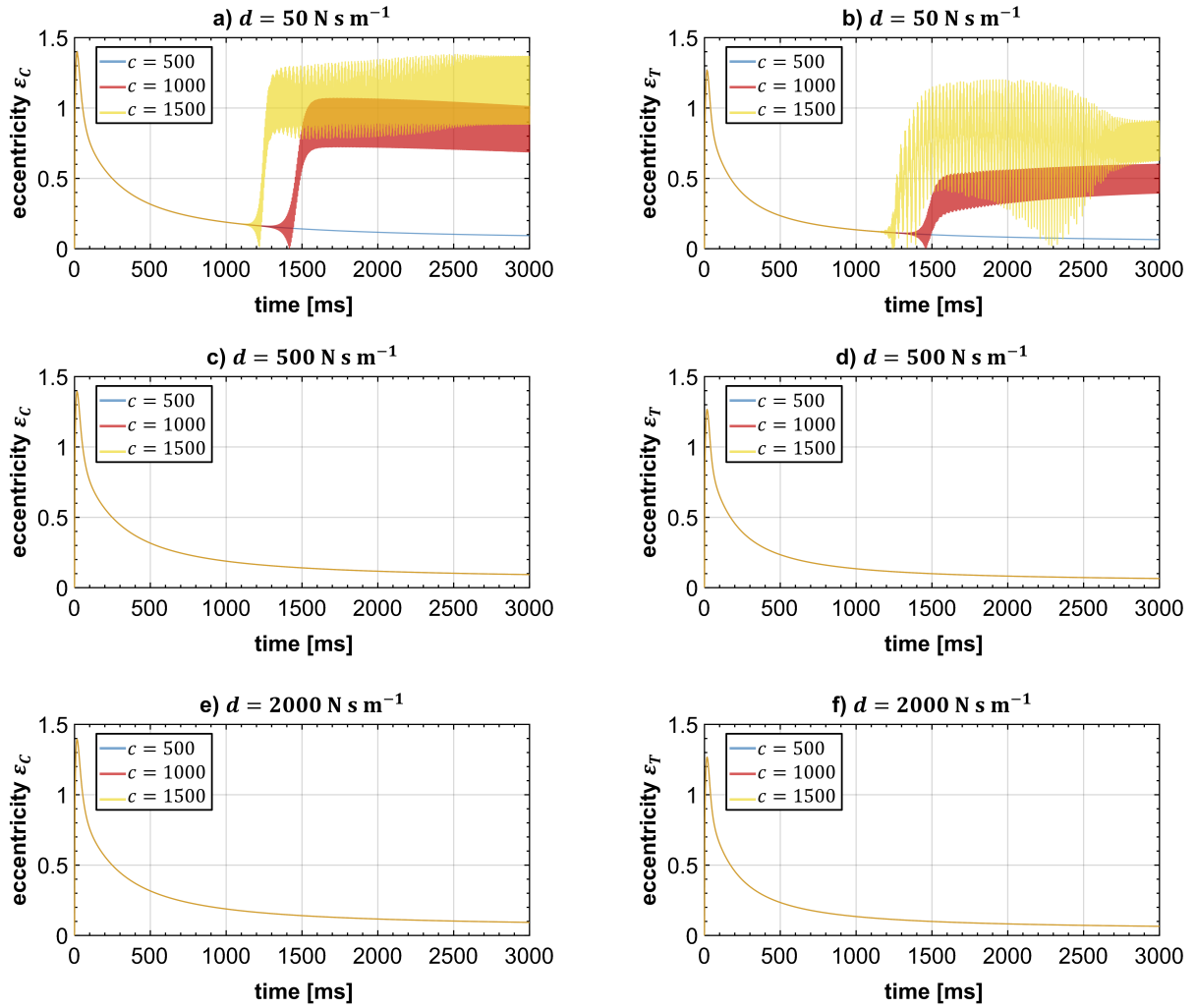


Fig. 11. Case 2 ($C = 15 \mu\text{m}$, $\Delta H = 30 \mu\text{m}$), compressor- and turbine-side bearing eccentricities $\varepsilon_C(t)$ and $\varepsilon_T(t)$: (a)–(b) $d = 50 \text{ N s m}^{-1}$, (c)–(d) $d = 500 \text{ N s m}^{-1}$, (e)–(f) $d = 2000 \text{ N s m}^{-1}$

imbalance would be considered, also the rotor speed would be observed in the spectra.

Case 2: Equivalent simulations are carried out for $C = 15 \mu\text{m}$ and $\Delta H = 30 \mu\text{m}$, see Figs. 11 and 12. The results are quite similar to the former case. Now, the simulations with $c = 1500 \text{ N mm}^{-1}$ and $c = 1000 \text{ N mm}^{-1}$ in combination with the damping coefficient $d = 50 \text{ N s m}^{-1}$ exhibit the dangerous *bifurcation path 1*.

Case 3: Simulation results for $C = 20 \mu\text{m}$ and $\Delta H = 40 \mu\text{m}$ are depicted in Figs. 13 and 14. The stability behavior is similar to case 2 with one exception: for $c = 500 \text{ N mm}^{-1}$ and $d = 50 \text{ N s m}^{-1}$, *bifurcation path 2a* is observed.

Case 4: Finally, the bearing parameters $C = 30 \mu\text{m}$ and $\Delta H = 60 \mu\text{m}$ are considered, see Figs. 15 and 16. For $d = 50 \text{ N s m}^{-1}$, all three simulations exhibit the problematic *bifurcation path 1*. With the larger damping coefficient $d = 500 \text{ N s m}^{-1}$, the simulation with the low stiffness of $c = 500 \text{ N mm}^{-1}$ is stable in the complete speed range. The simulation with the parameters $c = 1000 \text{ N mm}^{-1}$ and $d = 500 \text{ N s m}^{-1}$ exhibits a Hopf bifurcation at $t \approx 1800 \text{ ms}$ into *bifurcation path 2a*. For $c = 1500 \text{ N mm}^{-1}$ and $d = 500 \text{ N s m}^{-1}$, *bifurcation path 1* is observed. The simulations with the large damping coefficient $d = 2000 \text{ N s m}^{-1}$ show *bifurcation path 2a*. Due to the large damping, the amplitudes of the whirl/whip are not decreasing with

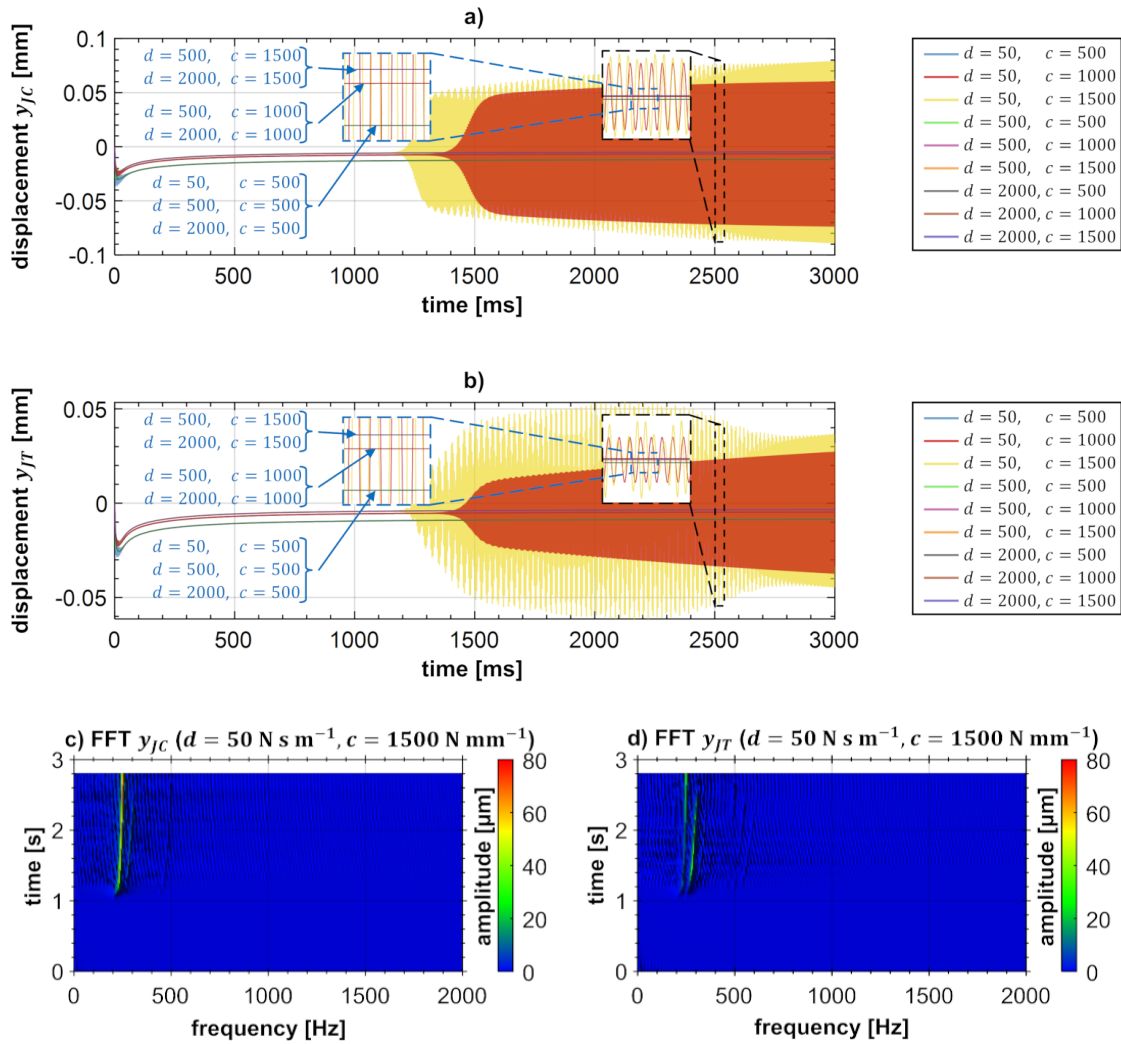


Fig. 12. Case 2 ($C = 15 \mu\text{m}$, $\Delta H = 30 \mu\text{m}$): (a)–(b) compressor and turbine-side rotor displacements $y_{JC}(t)$ and $y_{JT}(t)$, (c)–(d) frequency spectra of $y_{JC}(t)$ and $y_{JT}(t)$ for the parameters $d = 50 \text{ N s m}^{-1}$ and $c = 1500 \text{ N mm}^{-1}$

increasing rotor speed.

An overview on the influence of the stiffness and damping coefficients c and d on the stability and bifurcation behavior of the rotor/bearing system is presented in Fig. 17 in the form of bifurcation maps. As can be seen, the smaller the bearing clearance gets, the larger becomes the stable region. Furthermore, two basic trends may be observed in the stability/bifurcation plots:

- (i) Increasing the stiffness c , the risk of reaching the dangerous bifurcation path 1 increases (especially for smaller values of d).
- (ii) Increasing the damping d (so that the system might even become overdamped), the possibility increases that the system bifurcates into bifurcation path 2a. The whirl/whip amplitudes generally remain moderate so that the system can be operated securely within bifurcation path 2a.

Case study on the step height ΔH : In Fig. 18, a case study for $C = 15 \mu\text{m}$ and $c = 1000 \text{ N mm}^{-1}$ is presented and the influence of the step height ΔH is investigated. As can be seen, for $\Delta H = 0$ all simulations become unstable at very low rotor speeds. Hence, bearing

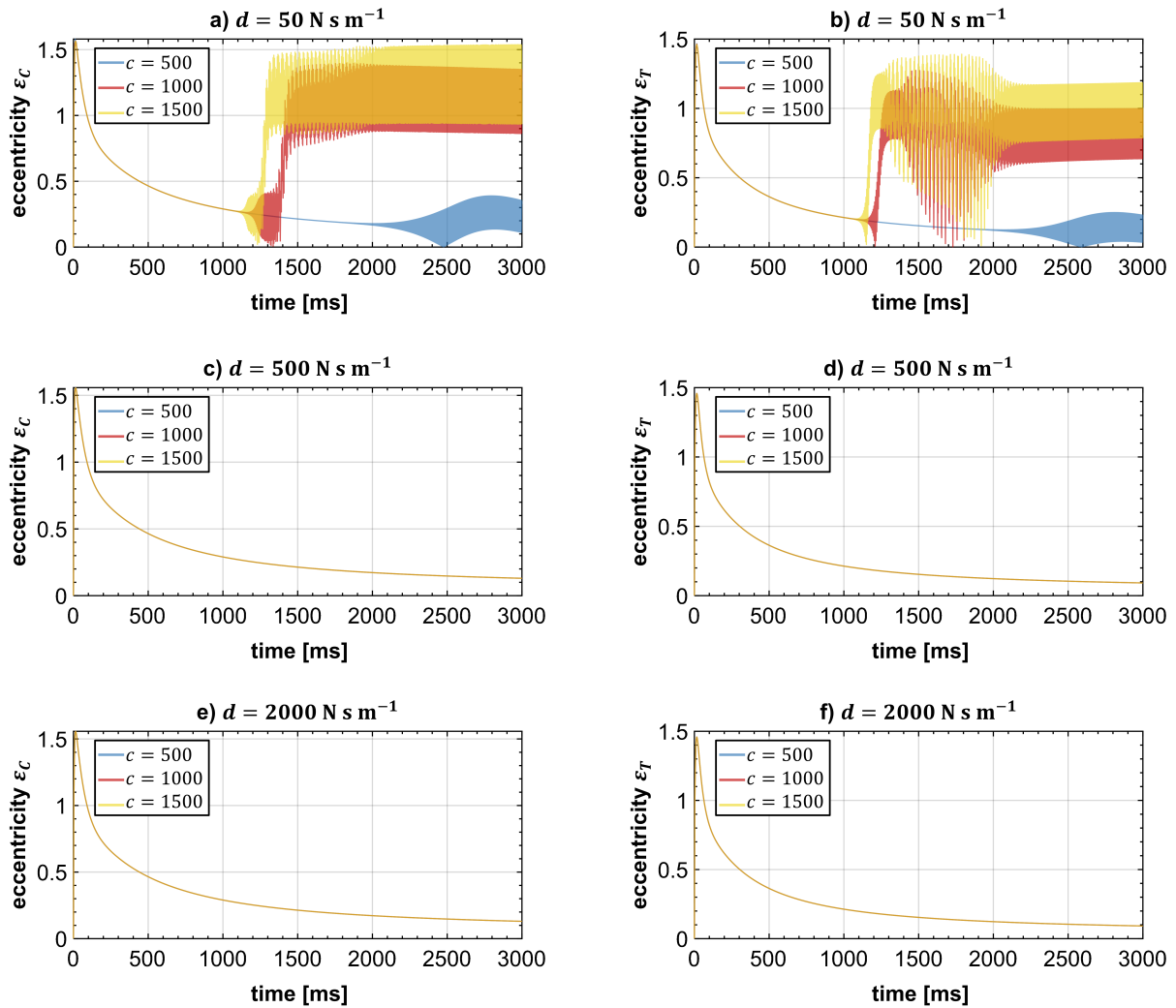


Fig. 13. Case 3 ($C = 20 \mu\text{m}$, $\Delta H = 40 \mu\text{m}$), compressor- and turbine-side bearing eccentricities $\varepsilon_C(t)$ and $\varepsilon_T(t)$: (a)–(b) $d = 50 \text{ N s m}^{-1}$, (c)–(d) $d = 500 \text{ N s m}^{-1}$, (e)–(f) $d = 2000 \text{ N s m}^{-1}$

geometries with $\Delta H = 0$ – and also bearing geometries with a plain circular bearing geometry (not shown here) – are from the practical point of view of no interest. For $\Delta H = 15 \mu\text{m}$, the simulation with $d = 50 \text{ N s m}^{-1}$ exhibits the dangerous *bifurcation path 1*, while the run-up simulation with the larger damping $d = 500 \text{ N s m}^{-1}$ is stable in the entire speed range. Similar results are observed for the case $\Delta H = 30 \mu\text{m}$ and $\Delta H = 45 \mu\text{m}$: the bearing eccentricities for the simulations with $d = 50 \text{ N s m}^{-1}$ are smaller compared to the simulation with $\Delta H = 15 \mu\text{m}$.

Summary: Air ring bearings with small clearances C show a very good stability behavior even for larger values of c and smaller values d . If very small bearing clearances cannot be realized for practical/technical reasons (e.g., problems due to thermal expansion, manufacturing costs), an increase of d or a decrease of c may enable a stable rotor operation (or at least self-excited vibrations with moderate and technically uncritical amplitudes). However, if d is chosen too large, overdamping may occur, which can yield large and critical amplitudes. The run-up simulations also show that the step height ΔH should be chosen properly, i.e., not too small.

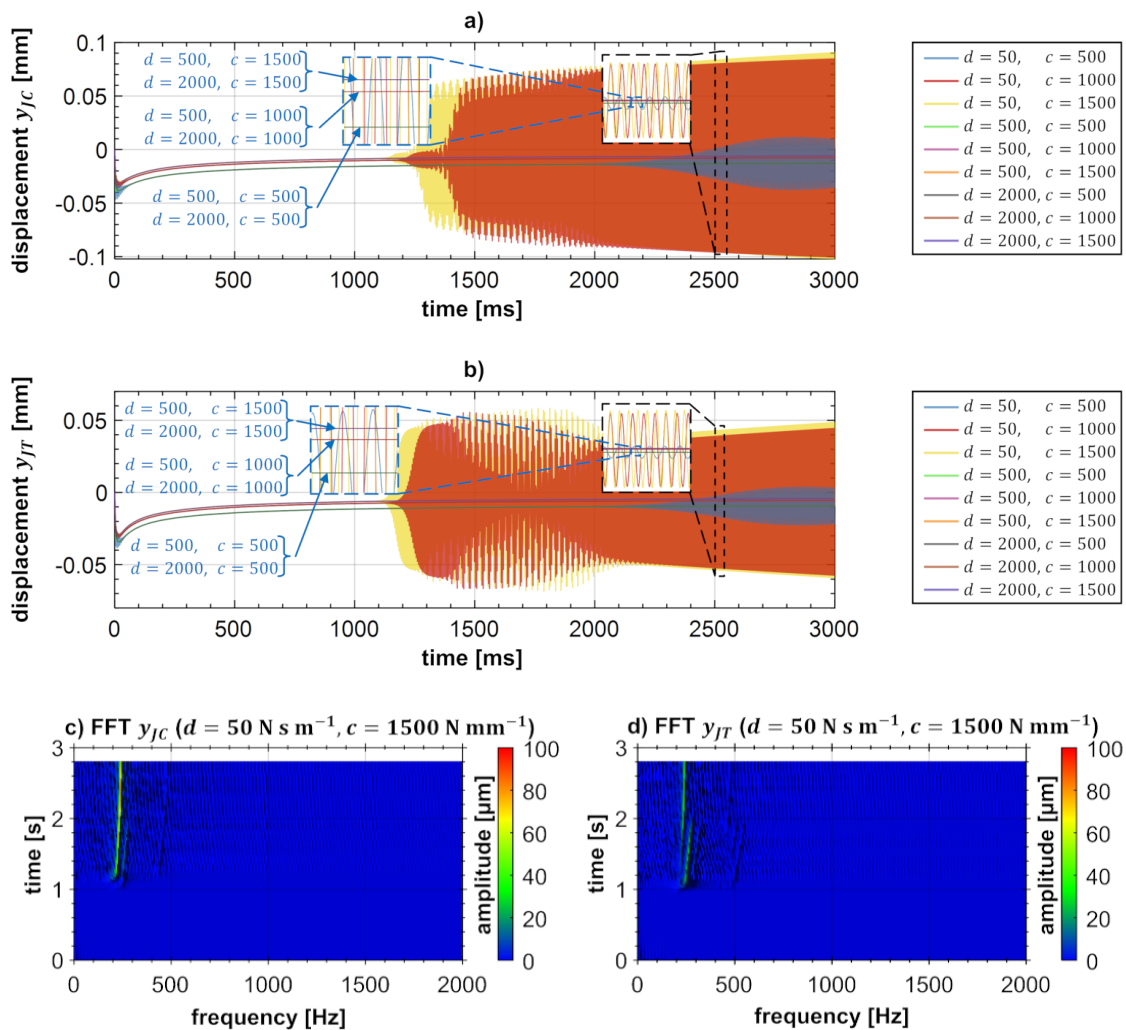


Fig. 14. Case 3 ($C = 20 \mu\text{m}$, $\Delta H = 40 \mu\text{m}$): (a)–(b) compressor and turbine-side rotor displacements $y_{JC}(t)$ and $y_{JT}(t)$, (c)–(d) frequency spectra of $y_{JC}(t)$ and $y_{JT}(t)$ for the parameters $d = 50 \text{ N s m}^{-1}$ and $c = 1500 \text{ N mm}^{-1}$

5. Conclusion

Air ring bearings might be considered as a further development of rigid air bearings. The idea is to connect the bearing bushing – i.e., the bushing ring – elastically with the housing. Therefore, an elastomer might be used or a foil structure. Here, a visco-elastically mounting of the bushing ring has been considered. The ring mounting also introduces external damping to the system, which can significantly improve the performance of the rotor/bearing system. The inner surface of the ring considered here has a three-lobed geometry.

Properly choosing the bearing parameters, air ring bearings might be an interesting alternative to classical air foil bearings. Considering air foil bearings, they often suffer from wear occurring in the top foil coating. As a consequence, the mechanical behavior of the bearing will change during operation and the number of start/stop operations is usually limited. Furthermore, the lift-off speed and power loss of foil bearings are comparatively large compared to rigid air bearings.

Air ring bearings also have different advantages compared to rigid herringbone bearings. A main advantage of herringbone bearings is their excellent stability behavior (stable operation

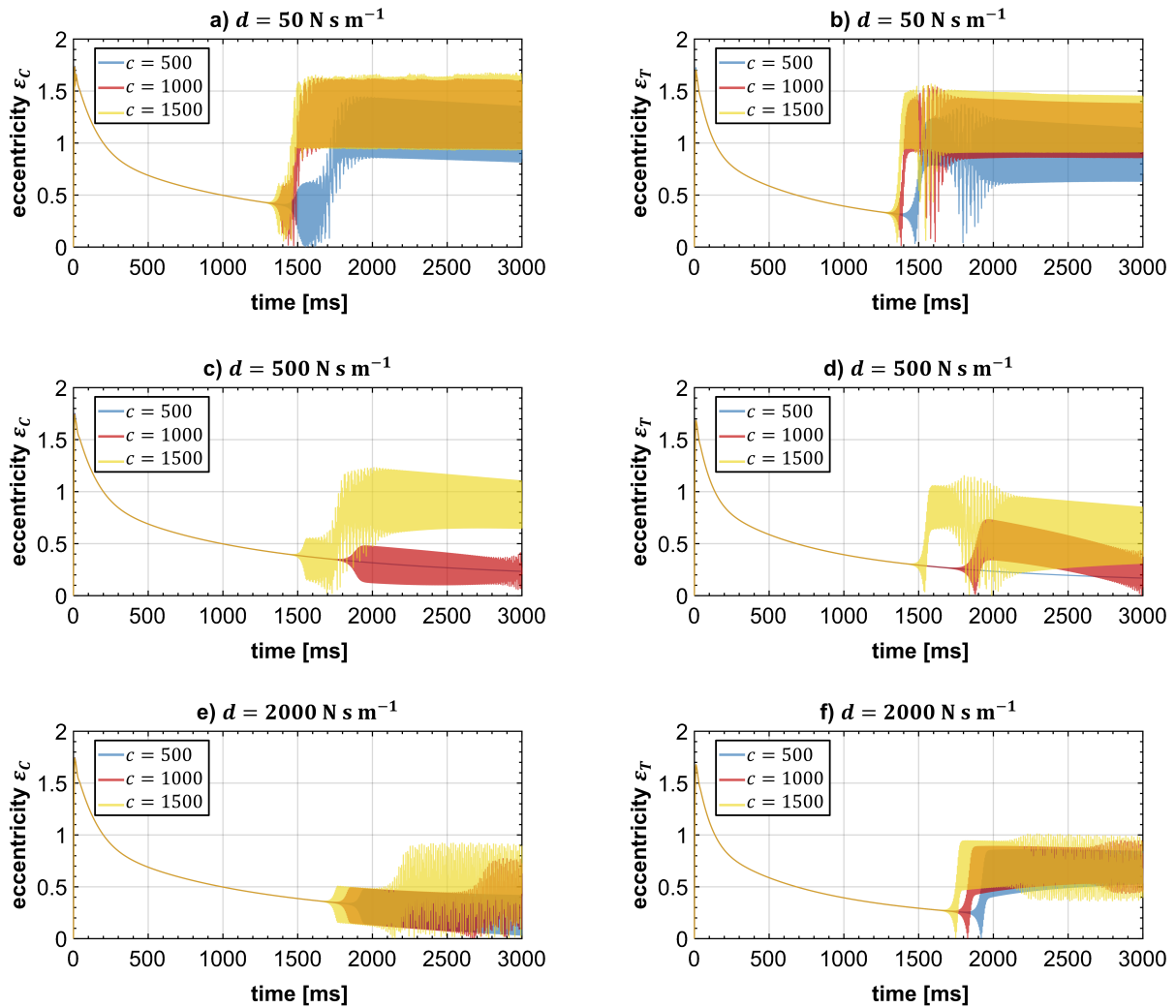


Fig. 15. Case 4 ($C = 30 \mu\text{m}$, $\Delta H = 60 \mu\text{m}$), compressor- and turbine-side bearing eccentricities $\epsilon_C(t)$ and $\epsilon_T(t)$: (a)–(b) $d = 50 \text{ N s m}^{-1}$, (c)–(d) $d = 500 \text{ N s m}^{-1}$, (e)–(f) $d = 2000 \text{ N s m}^{-1}$

in the complete speed range). Therefore, very small bearing clearances are required and in consequence a rather expensive thermo-management. A very good stability and vibration behavior may also be achieved with air ring bearings. Especially for smaller bearing clearances, a stable operation in the complete speed range can be achieved. Rotors in air ring bearings may – in contrast to rotors in rigid herringbone bearings – however also be operated above the linear threshold speed of instability. By properly choosing the stiffness and damping properties of the ring supporting structure, stable self-excited oscillations with moderate amplitudes may be obtained (bifurcation path 2a) even for larger bearing clearances so that an elaborate thermo-management will not be necessary.

Rotors supported in air ring bearings may therefore be considered as rather robust systems. In a wide parameter range, the system is completely stable (the rotor runs in a stable equilibrium position) or self-excited oscillations with technically harmless amplitudes occur (bifurcation path 2a). The system can, however, not be operated within bifurcation paths 1 and 2b, since the amplitudes usually exceed critical values, which prevents a secure operation.

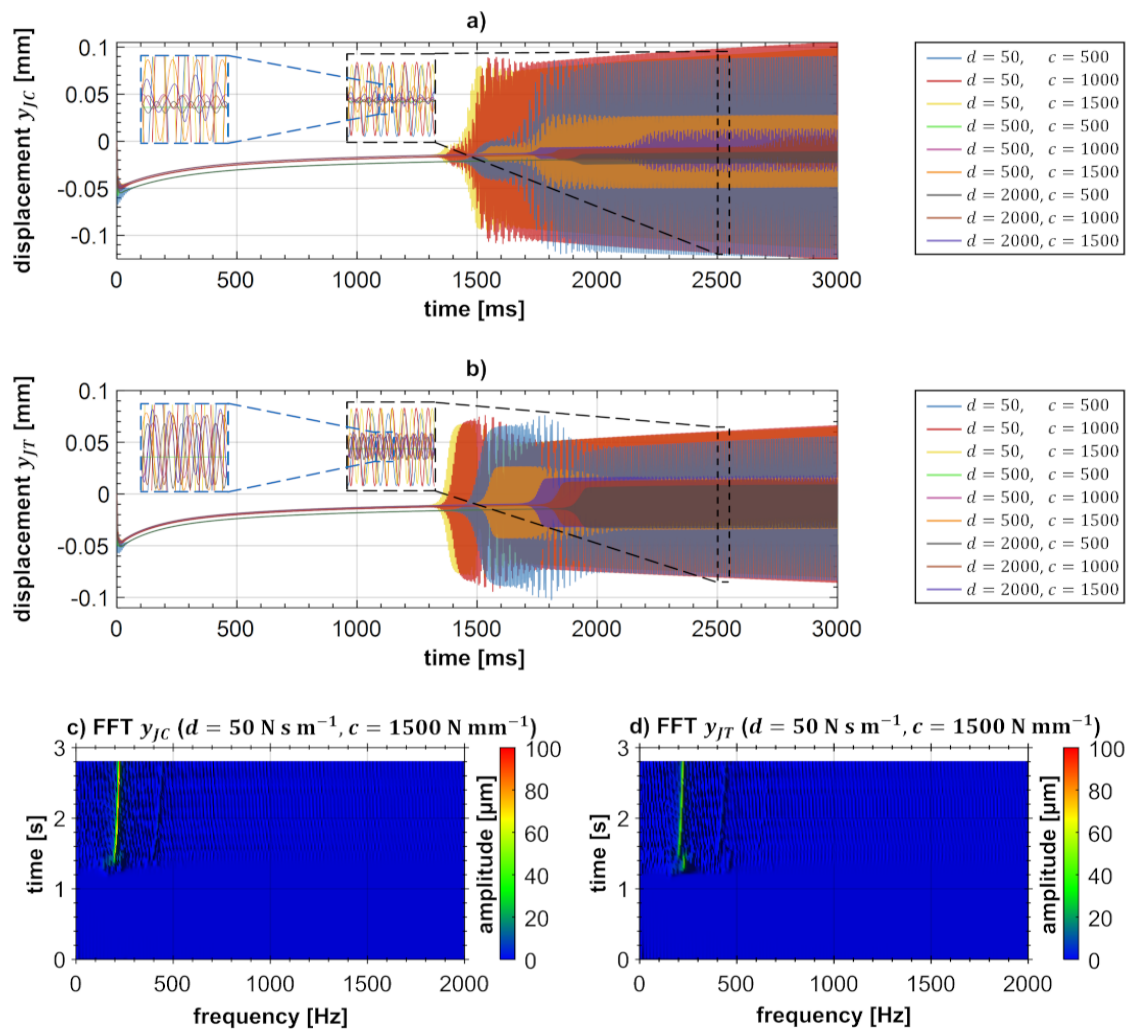


Fig. 16. Case 4 ($C = 30 \mu\text{m}$, $\Delta H = 60 \mu\text{m}$): (a)–(b) compressor and turbine-side rotor displacements $y_{JC}(t)$ and $y_{JT}(t)$, (c)–(d) frequency spectra of $y_{JC}(t)$ and $y_{JT}(t)$ for the parameters $d = 50 \text{ N s m}^{-1}$ and $c = 1500 \text{ N mm}^{-1}$

References

- [1] Al-Bender, F., Air bearings: Theory, design and applications, John Wiley & Sons, 2021. <https://doi.org/10.1002/9781118926444>
- [2] Arghir, M., Benchekroun, O., A new structural bump foil model with application from start-up to full operating conditions, Journal of Engineering for Gas Turbines and Power 141 (10) (2019) 1–12. <https://doi.org/10.1115/1.4044685>
- [3] Arghir, M., Benchekroun, O., A simplified structural model of bump-type foil bearings based on contact mechanics including gaps, Tribology International 134 (2019) 129–144. <https://doi.org/10.1016/j.triboint.2019.01.038>
- [4] Balducchi, F., Arghir, M., Gauthier, R., Experimental analysis of the unbalance response of rigid rotors supported on aerodynamic foil bearings, Journal of Vibration and Acoustics 137 (6) (2015) 1–11. <https://doi.org/10.1115/1.4031409>
- [5] Bättig, P., Schiffmann, J., Unstable tilting motion of flexibly supported gas bearing bushings, Mechanical Systems and Signal Processing 162 (2022) 1–17. <https://doi.org/10.1016/j.ymssp.2021.107981>

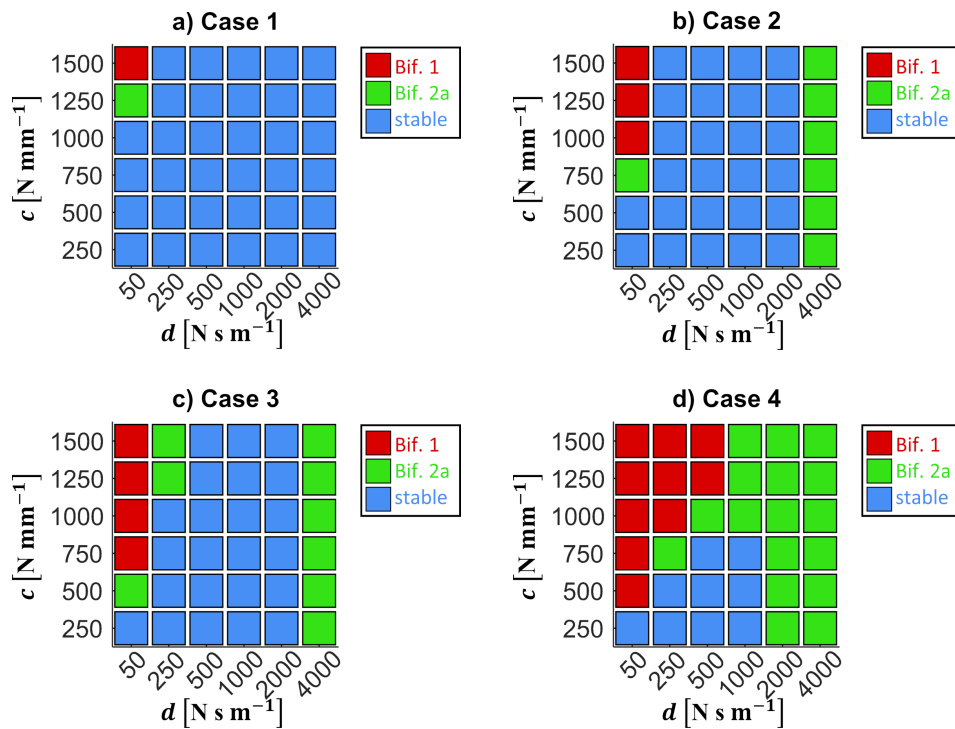


Fig. 17. Bifurcation maps. Influence of the damping and stiffness coefficients d and c on the bifurcation behavior of the system: (a) case 1, (b) case 2, (c) case 3, (d) case 4

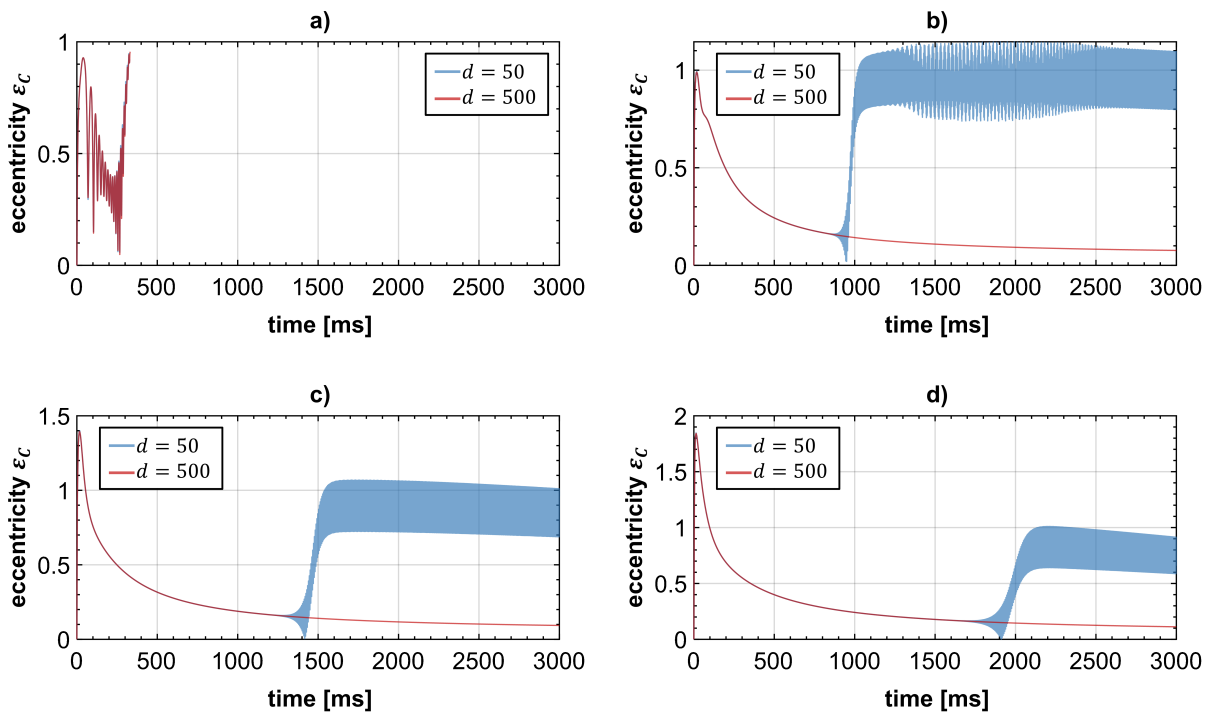


Fig. 18. Case study on different step heights ΔH with $C = 15 \mu\text{m}$, $c = 1000 \text{ N mm}^{-1}$, compressor-side dimensionless bearing eccentricity $\varepsilon_C(t)$ with: (a) $\Delta H = 0 \mu\text{m}$, (b) $\Delta H = 15 \mu\text{m}$, (c) $\Delta H = 30 \mu\text{m}$, (d) $\Delta H = 45 \mu\text{m}$

- [6] Bättig, P. K., Wagner, P. H., Schiffmann, J. A., Experimental investigation of enhanced grooves for herringbone grooved journal bearings, *Journal of Tribology* 144 (9) (2022) 1–12. <https://doi.org/10.1115/1.4053978>
- [7] Bonello, P., Bin Hassan, M. F., An experimental and theoretical analysis of a foil-air bearing rotor system, *Journal of Sound and Vibration* 413 (2018) 395–420. <https://doi.org/10.1016/j.jsv.2017.10.036>
- [8] Dobrica, M. B., Fillon, M., Mixed lubrication, In: *Encyclopedia of tribology*, (eds) Q. J. Wang, Y.-W. Chung, Boston, Springer, 2013. https://doi.org/10.1007/978-0-387-92897-5_27
- [9] Feng, K., Zhao, X., Guo, Z., Design and structural performance measurements of a novel multi-cantilever foil bearing, *Proceedings of the Institution of Mechanical Engineers, Part C: Journal of Mechanical Engineering Science* 229 (10) (2015) 1830–1838. <https://doi.org/10.1177/0954406214547529>
- [10] Fleming, D. P., Hamrock, B. J., Optimization of self-acting herringbone journal bearing for maximum stability, NASA Technical Note D-6351, Washington, 1973.
- [11] Gear, C. W., Gupta, G. K., Leimkuhler, B. J., Automatic integration of the Euler-Lagrange equations with constraints, *Journal of Computational and Applied Mathematics* 12–13 (1985) 77–90. [https://doi.org/10.1016/0377-0427\(85\)90008-1](https://doi.org/10.1016/0377-0427(85)90008-1)
- [12] Gomes, C., Thule, C., Broman, D., Larsen, P. G., Vangheluwe, H., Co-simulation: A survey, *ACM Computing Surveys* 51 (3) (2018) 1–33. <https://doi.org/10.1145/3179993>
- [13] Gu, L., Guenat, E., Schiffmann, J., A review of grooved dynamic gas bearings, *Applied Mechanics Reviews* 72 (2020) 1–15. <https://doi.org/10.1115/1.4044191>
- [14] Haug, E. J., *Computer-aided kinematics and dynamics of mechanical systems*, Allyn and Bacon, Boston, 1989.
- [15] Heshmat, H., Shapiro, W., Gray, S., Development of foil journal bearings for high load capacity and high speed whirl stability, *Journal of Lubrication Technology* 104 (2) (1982) 149–156. <https://doi.org/10.1115/1.3253173>
- [16] Hoffmann, R., Liebich, R., Characterisation and calculation of nonlinear vibrations in gas foil bearing systems—An experimental and numerical investigation, *Journal of Sound and Vibration* 412 (2018) 389–409. <https://doi.org/10.1016/j.jsv.2017.09.040>
- [17] Iseli, E., Schiffmann, J., Stability and unbalance analysis of rigid rotors supported by spiral groove bearings: Comparison of different approaches, *Journal of Engineering for Gas Turbines and Power* 143 (12) (2021) 1–12. <https://doi.org/10.1115/1.4052025>
- [18] Khonsari, M. M., Booser, E. R., *Applied tribology: Bearing design and lubrication*, John Wiley & Sons, 2008. <https://doi.org/10.1002/9780470059456>
- [19] Larsen, J. S., Santos, I. F., On the nonlinear steady-state response of rigid rotors supported by air foil bearings—Theory and experiments, *Journal of Sound and Vibration* 346 (2015) 284–297. <https://doi.org/10.1016/j.jsv.2015.02.017>
- [20] Mahner, M., Bauer, M., Lehn, A., Schweizer, B., An experimental investigation on the influence of an assembly preload on the hysteresis, the drag torque, the lift-off speed and the thermal behavior of three-pad air foil journal bearings, *Tribology International* 137 (2019) 113–126. <https://doi.org/10.1016/j.triboint.2019.02.026>
- [21] Mahner, M., Bauer, M., Schweizer, B., Numerical analyzes and experimental investigations on the fully-coupled thermo-elasto-gasdynamic behavior of air foil journal bearings, *Mechanical Systems and Signal Processing* 149 (2021) 1–32. <https://doi.org/10.1016/j.ymsp.2020.107221>
- [22] Mahner, M., Li, P., Lehn, A., Schweizer, B., Numerical and experimental investigations on preload effects in air foil journal bearings, *Journal of Engineering for Gas Turbines and Power* 140 (3) (2018) 1–9. <https://doi.org/10.1115/1.4037965>
- [23] Malanoski, S. B., Experiments on an ultrastable gas journal bearing, *Journal of Lubrication Technology* 89 (4) (1967) 433–438. <https://doi.org/10.1115/1.3617021>

- [24] Meyer, T., Kraft, J., Schweizer, B., Co-simulation: Error estimation and macro-step size control, *Journal of Computational and Nonlinear Dynamics* 16 (4) (2021) 1–26. <https://doi.org/10.1115/1.4048944>
- [25] Michel, H., Liebich, R., Challenges in validating a thermo-hydrodynamic gas foil bearing model, *Journal of Engineering for Gas Turbines and Power* 143 (4) (2021) 1–13. <https://doi.org/10.1115/1.4047769>
- [26] Miyanaga, N., Tomioka, J., Effect of support stiffness and damping on stability characteristics of herring-bone-grooved aerodynamic journal bearings mounted on viscoelastic supports, *Tribology International* 100 (2016) 195–203. <https://doi.org/10.1016/j.triboint.2016.01.019>
- [27] Papafragkos, P., Gavalas, I., Raptopoulos, I., Chasalevris, A., Optimizing energy dissipation in gas foil bearings to eliminate bifurcations of limit cycles in unbalanced rotor systems, *Nonlinear Dynamics* 111 (2023) 67–95. <https://doi.org/10.1007/s11071-022-07837-1>
- [28] Samanta, P., Murmu, N. C., Khonsari, M. M., The evolution of foil bearing technology, *Tribology International* 135 (2019) 305–323. <https://doi.org/10.1016/j.triboint.2019.03.021>
- [29] San Andrés, L., Chirathadam, T. A., A metal mesh foil bearing and a bump-type foil bearing: Comparison of performance for two similar size gas bearings, *Journal of Engineering for Gas Turbines and Power* 134 (10) (2012) 1–13. <https://doi.org/10.1115/1.4007061>
- [30] San Andrés, L., Kim, T. H., Thermohydrodynamic analysis of bump type gas foil bearings: A model anchored to test data, *Journal of Engineering for Gas Turbines and Power* 132 (4) (2010) 1–10. <https://doi.org/10.1115/1.3159386>
- [31] Schweizer, B., Lu, D., Semi-implicit co-simulation approach for solver coupling, *Archive of Applied Mechanics* 84 (12) (2014) 1739–1769. <https://doi.org/10.1007/s00419-014-0883-5>
- [32] Shabana, A. A., *Dynamics of multibody systems*, Cambridge University Press, 2005. <https://doi.org/10.1017/CBO9780511610523>
- [33] Simeon, B., *Computational flexible multibody dynamics: A differential-algebraic approach*, Springer Berlin, Heidelberg, 2013. <https://doi.org/10.1007/978-3-642-35158-7>
- [34] Somaya, K., Okubo, K., Miyatake, M., Yoshimoto, S., Threshold speed of instability of a herringbone-grooved rigid rotor with a bearing bush flexibly supported by straight spring wires, *Proceedings of the ASME Turbo Expo 2015: Turbine Technical Conference and Exposition Volume 7A: Structures and Dynamics*, Montreal, ASME, 2015, pp. 1–9. <https://doi.org/10.1115/GT2015-43161>
- [35] Song, J.-H., Kim, D., Foil gas bearing with compression springs: Analyses and experiments, *Journal of Tribology* 129 (3) (2007) 628–639. <https://doi.org/10.1115/1.2736455>
- [36] Swanson, E. E., Shawn O’Meara, P., The wing foil: A novel compliant radial foil bearing design, *Journal of Engineering for Gas Turbines and Power* 140 (8) (2018) 1–7. <https://doi.org/10.1115/1.4038366>
- [37] Szeri, A. Z., *Fluid film lubrication: Theory and design*, Cambridge University Press, 2005.
- [38] Tatara, A., Koike, H., Iwasaki, A., The stability of flexibly supported, externally pressurized gas journal bearings: Case of a rigid rotor, *Bulletin of JSME* 16 (100) (1973) 1573–1579. <https://doi.org/10.1299/jsme1958.16.1573>
- [39] Vohr, J. H., Chow, C. Y., Characteristics of herringbone-grooved, gas-lubricated journal bearings, *Journal of Basic Engineering* 87 (3) (1965) 568–576. <https://doi.org/10.1115/1.3650607>
- [40] Waumans, T., Peirs, J., Al-Bender, F., Reynaerts, D., Aerodynamic journal bearing with a flexible, damped support operating at 7.2 million DN, *Journal of Micromechanics and Microengineering* 21 (2011) 1–12. <https://doi.org/10.1088/0960-1317/21/10/104014>
- [41] Zeise, P., Schweizer, B., Dynamics, stability and bifurcation analysis of rotors in air ring bearings, *Journal of Sound and Vibration* 521 (2022) 1–35. <https://doi.org/10.1016/j.jsv.2021.116392>